

# Coupled quantum mechanical/molecular mechanical modeling of the fracture of defective carbon nanotubes and graphene sheets

Roopam Khare,<sup>1</sup> Steven L. Mielke,<sup>2</sup> Jeffrey T. Paci,<sup>2</sup> Sulin Zhang,<sup>1</sup> Roberto Ballarini,<sup>3</sup> George C. Schatz,<sup>2,\*</sup> and Ted Belytschko<sup>1,†</sup>

<sup>1</sup>*Department of Mechanical Engineering, Northwestern University, Evanston, Illinois 60208-3111, USA*

<sup>2</sup>*Department of Chemistry, Northwestern University, Evanston, Illinois 60208-3113, USA*

<sup>3</sup>*Department of Civil Engineering, University of Minnesota, Minneapolis, Minnesota 55455, USA*

(Received 12 July 2006; revised manuscript received 29 November 2006; published 9 February 2007)

Coupled quantum mechanical/molecular mechanical (QM/MM) calculations were used to study the effects of large defects and cracks on the mechanical properties of carbon nanotubes and graphene sheets. The semi-empirical method PM3 was used to treat the QM subdomains and a Tersoff-Brenner potential was used for the molecular mechanics; some of the QM calculations were also done using density functional theory (DFT). Scaling of the Tersoff-Brenner potential so that the modulus and overall stress-strain behavior of the QM and MM models matched quite closely was essential for obtaining meaningful coupled calculations of the mechanical properties. The numerical results show that at the nanoscale, the weakening effects of holes, slits, and cracks vary only moderately with the shape of the defect, and instead depend primarily on the cross section of the defect perpendicular to the loading direction and the structure near the fracture initiation point. The fracture stresses for defective graphene sheets are in surprisingly good agreement with the Griffith formula for defects as small as 10 Å, which calls into question the notion of nanoscale flaw tolerance. The energy release rate at the point of crack extension in graphene was calculated by the  $J$ -integral method and exceeds twice the surface energy density by 10% for the QM(DFT)/MM results, which indicates a modest lattice trapping effect.

DOI: [10.1103/PhysRevB.75.075412](https://doi.org/10.1103/PhysRevB.75.075412)

PACS number(s): 68.65.-k, 62.25.+g, 61.50.Ah, 81.07.De

## I. INTRODUCTION

Due to their favorable mechanical properties, carbon nanotubes (CNTs) and exfoliated graphene sheets have attracted considerable interest as nanoreinforcements for polymer composites. Electronic structure calculations<sup>1-7</sup> of the mechanical behavior of pristine CNTs predict fracture strengths in the range of 75–135 GPa and ultimate strains of as much as 30%. However, manufacture of mass-quantities of perfect CNTs or graphene sheets may prove challenging; in practice, mechanical properties will often be limited by the presence of defects—in many cases of substantial size. Oxidative purification treatments<sup>8-10</sup> are commonly used in the production of CNTs and we have suggested<sup>6,11</sup> that these can result in pitting, which provides a plausible explanation for the deviations between the CNT strength measurements of Yu *et al.*<sup>12</sup> and theoretical predictions. One route for the exfoliation of graphene sheets involves thermal exfoliation of graphite oxide.<sup>13</sup> During this process approximately 30% of the carbon atoms are lost as CO<sub>2</sub>; thus, the resulting sheets are expected to be highly defected. A detailed understanding of the consequences of such defects may be crucial to the effective utilization of these materials.

Previous electronic structure calculations of defected CNTs were limited to small defects because of the high computational cost of QM calculations. Therefore, the studies<sup>6,14</sup> of larger defects were restricted to MM calculations. However, the modified<sup>15,16</sup> second generation<sup>17</sup> Tersoff-Brenner (MTB-G2) potential employed in those calculations tends to systematically underestimate the strength of both pristine and defected CNTs as compared to QM calculations, and has been shown<sup>3</sup> to predict qualitatively different mechanisms for the fracture of defected CNTs. Thus, a better understand-

ing of the role of defects in CNTs necessitates electronic structure calculations.

One way to treat a system of large molecules is to adopt linear scaling QM methods, which reduce the order of computation to  $O(N)$ , where  $N$  is the total number of orbitals. Another approach to treating large systems is to couple a QM method to an MM method so that the important regions of the system are treated quantum mechanically and MM interactions are used elsewhere. In fracture studies, only part of the system, such as the vicinity of defects, requires an accurate treatment of bond breaking; for such systems QM methods can be used for these regions and MM methods can be applied to the rest of the system. Although the MM potential does not need to be able to model bond fracture accurately, it must still predict stiffnesses and strengths that are consistent with the QM results; in the following we will present a simple scaling scheme to improve the compatibility of the QM and MM mechanical properties.

Here we describe a set of coupled quantum mechanical/molecular mechanical (QM/MM) calculations of the fracture of CNTs with large defects and the fracture of graphene sheets. We also consider the effect of lattice trapping<sup>18-21</sup> by calculating the energy release rate of a crack in a QM/MM model of a graphene sheet using the  $J$ -integral<sup>22</sup> method.

The rest of the paper is organized as follows. Section II gives an overview of the coupling method and its implementation. In Sec. III the results of fracture in the presence of defects such as one- and two-atom vacancy defects as well as nanosized holes and slits are presented. Section IV describes the results for lattice trapping in graphene sheets. Conclusions are given in Sec. V.

## II. METHOD

The coupled QM/MM method adopted here is a two-layer ONIOM scheme.<sup>23</sup> The MM interaction potential is a modified<sup>15</sup> version of a second generation Tersoff-Brenner<sup>17</sup> potential; in particular, the cutoff function is removed and instead interactions are only retained for atom-atom pairs that are separated by less than 2 Å in the initial (unstrained) configuration. The name MTB-G2 will be used to distinguish this version of the potential from the standard second generation reactive empirical bond order (REBO) potential, which retains the cutoff function. The use in fracture studies of REBO potentials in which the cutoff function is retained leads to qualitatively inaccurate behavior. Two types of QM interactions are considered: semi-empirical (PM3) calculations obtained with the GAMESS software package<sup>24</sup> and DFT calculations. The DFT calculations were performed using the Spanish initiative for electronic simulations with thousands of atoms (SIESTA) package.<sup>25,26</sup> The Perdew-Burke-Ernzerhof (PBE) GGA functional, a double- $\zeta$  plus polarization basis set, and Troullier-Martins<sup>27,28</sup> pseudopotentials were used. Core radii of 1.15 and 1.25  $a_0$  were used for carbon and hydrogen, respectively, and a nonlinear exchange-correlation correction pseudocore radius of 1.50  $a_0$  was used for carbon. Periodic boundary conditions were employed for the calculation of the surface energy density, whereas cluster calculations were used for the remaining DFT calculations. The  $\Gamma$  point was used for Brillouin zone sampling and diagonalization to solve the Kohn-Sham equations. We used spin-restricted QM calculations for all of the work presented here. Spin unrestricted calculations are generally more accurate but they are more time consuming, difficult to converge, and are subject to issues of spin contamination which would need to be carefully assessed before they should be used. For our present goals of testing QM/MM methods spin restricted calculations will suffice.

ONIOM<sup>23</sup> is a widely-used method for coupling in QM/MM calculations due to its simplicity of implementation. It is a general framework that combines layers of computational methods of different levels of accuracy. In the two-layer ONIOM scheme employed here, the energy is given by

$$E = E^{\text{MM}} + E_{\text{F}}^{\text{QM}} - E_{\text{F}}^{\text{MM}}, \quad (1)$$

where  $E^{\text{MM}}$  is the MM energy of the entire system, and  $E_{\text{F}}^{\text{QM}}$  and  $E_{\text{F}}^{\text{MM}}$  are, respectively, the QM and MM energies of a special subdomain, hereafter usually just referred to as either the QM subdomain or simply the “fragment”, within which accurate treatment of bond behavior is desired. The complement of this region will occasionally be referred to as the MM subdomain.

In calculations for the fragment we employed hydrogen link atoms to saturate the dangling bonds created by cutting covalent bonds that straddle the interface. The link atoms were positioned to lie 1.09 Å along the vector connecting a boundary QM atom and its nearest neighbor across the boundary. The positions of the link atoms were not included in the degrees of freedom of the molecule and were not part of the geometry optimization. The use of hydrogen link at-

oms to terminate the dangling bonds of a fragment domain consisting of a conjugated graphitic network significantly alters the bond orders of the C–C bonds near the boundary and this can alter properties further inside the domain. To judge the errors introduced by this complication, we repeated our calculations with larger fragments and only report results where the error due to domain truncation is less than 10%.

The energy is minimized by a variable-metric function-minimization routine<sup>29</sup> to obtain the optimized geometry. In the computations reported here, the end carbon atoms of the model were displaced axially with a strain increment of 0.5% until fracture occurred. The end carbon atoms were constrained to a plane. The tensile strain is defined as

$$\varepsilon = \frac{\Delta l}{l}, \quad (2)$$

where  $l$  is the initial length of the specimen and  $\Delta l$  is the change in the length. Note that this definition, which corresponds to engineering strain, is not an appropriate general definition of strain for the large deformations obtained here; but because we are only concerned with axial deformation, it is adequate (see Belytschko *et al.*<sup>30</sup>). At each strain increment the tube configuration was optimized.

The numerical procedure at each strain increment can be summarized as follows:

- (1) Calculate the MM energy of the full system.
- (2) Calculate the QM and the MM energy of the fragment capped with the link atoms.
- (3) Calculate the energy of the system using Eq. (1).
- (4) Check the convergence criterion,  $\max|\text{gradient}| < \epsilon$ . If the convergence criterion is satisfied, the configuration is considered an equilibrium configuration, otherwise update the atomic positions and repeat from (1).

Where possible, we made use of approximate Hessian information and starting orbitals for the QM energy evaluations that were available from the prior strain steps. Once the geometry is optimized at a certain applied strain, the tensile stress in the tube is calculated as the sum of the axial components of the forces on the carbon atoms at one end of the CNT divided by the cross-sectional area,

$$\sigma_z = \frac{\sum_{\alpha=1}^m F_{\alpha z}}{\pi D t}, \quad (3)$$

where  $m$  is the number of carbon atoms at one end of the tube,  $F_{\alpha z}$  is the axial force on atom  $\alpha$ ,  $D$  is the current diameter of the tube, and  $t=3.4$  Å is a nominal value of the thickness of the CNTs (taken to be the interlayer spacing in graphite). Note that all of our calculations are for the true stress, so the diameter is a strain dependent parameter. Wherever possible, we obtain the value of the CNT diameter from an undefected region of the fragment subdomain because the QM and MM methods predict significantly different Poisson’s ratios and the goal of the QM/MM calculations is to match the results of pure QM calculations as closely as possible. Assuming a nominal thickness to define stress is a standard procedure for monolayer atomic sheets such as graphene and CNTs; a more unambiguous definition is based

on a force per linear dimension, see Arroyo and Belytschko.<sup>31,32</sup>

It is crucial in coupled QM/MM simulations of fracture that the MM model matches the QM model over a large range of strains; the upper end of this range should be near the fracture stress. Otherwise, various types of spurious phenomena occur which are simply a result of strength and stiffness mismatch between the QM and MM models. For example, if the strength of the MM model is less than that of the QM model, fracture can occur in the MM subdomain, even if the MM subdomain does not contain a defect and the QM subdomain does. Another consequence of such a mismatch occurs when a crack attempts to grow into a QM fragment from the MM subdomain: the crack can be deflected back into the MM model if the QM model is stiffer than the MM model.

These mismatches are of concern here because the standard MTB-G2 potential is significantly less stiff and weaker than the PM3 model. For example, for a [5,5] CNT containing a Stone-Wales (SW) defect<sup>33</sup> as reported in Mielke *et al.*,<sup>6</sup> the fracture stress calculated by pure QM calculations is 115 GPa, whereas the fracture stress of a [5,5] pristine tube obtained by MM calculations is 105 GPa. Consequently, if a QM/MM method is used with a QM treatment around the SW defect, the pristine part of the CNT will fail before the defective QM fragment.

To avoid these anomalies, the MTB-G2 energy was scaled so that the low-strain Young's modulus for a CNT closely matches that obtained from a QM calculation. For the armchair CNTs, the scaling factor was chosen to be 1.4 and for the zigzag CNTs the scaling factor was chosen to be 1.2. Similarly, the scaling factor for a graphene sheet was chosen to be 1.4 for QM(PM3)/MM calculations and 1.2 for QM(DFT)/MM calculations.

Our main justification for the scaling is that it matches the MM model more closely to the QM model at lower stresses. Since the fracture properties of the tube are governed by the region encapsulating the defect, which is treated quantum mechanically, the calculated strength is not affected much by the scaling of the MM potential. Another justification for the scaling is the fact that we have found for the quantum fragments used here, the results converge (i.e., the difference between successively larger fragments decrease). Furthermore, the results of the QM/MM calculations tend to the results of the pure QM calculations. However, we were not able to establish this trend for the largest models we used because pure QM calculations for these were beyond our resources.

Griffith's criterion<sup>34</sup> for fracture in brittle materials states that a crack will extend when the strain energy released by such extension exceeds the energy needed to create a newly fractured surface. This is a thermodynamic criterion and can be used to predict a rigorous lower bound for the fracture stress as a function of the crack length. For the special case of a linear elastic material, the fracture stress for a crack in a thin finite sheet of width  $w$  is given by<sup>35</sup>

$$\sigma_f = \sqrt{\frac{2Y\gamma}{\pi a} \cos\left(\frac{\pi a}{w}\right)}, \quad (4)$$

where  $a$  is the size of the defect (half-length of the crack) and  $a \ll w$ ,  $Y$  is Young's modulus, and  $\gamma$  is the surface energy

density. Note that graphene is nonlinear, so Eq. (4) is only an approximation to the Griffith stress.

The appropriate  $\gamma$  to use<sup>19</sup> in calculations of the Griffith formula is the work per unit area needed to *reversibly* separate the fracture surfaces. Thus, it includes contributions from relaxation of the fragments. The unrelaxed surface energy density for such calculations has been used previously,<sup>36-38</sup> and may provide a better estimate of the true fracture stress. However, the relaxed surface energy provides the proper basis from which to judge the contributions of lattice trapping effects. Our values of  $\gamma$  are obtained by dividing the difference between the energy of a pristine material at its optimized geometry and the energy of the two fragments after they are fractured along the desired surface, separated to infinity, and subsequently optimized to yield their equilibrium geometries, by twice the surface area (where the factor of two is included because fracture leads to two surfaces).

### III. RESULTS AND DISCUSSION

#### A. Small defects

We begin by studying the effects of small defects, one- or two-atom vacancy defects and a Stone-Wales defect,<sup>6</sup> on the mechanical strength of small CNTs such as [5,5] armchair and [10,0] zigzag tubes. The purpose of these computations was to examine how well the QM/MM calculations reproduce the results of pure QM calculations. The QM results were therefore considered as "benchmark" results, with the difference between the QM/MM and the QM computation indicating errors due to coupling. QM/MM methods are ubiquitous in many areas of chemistry but they are much less common for the study of fracture,<sup>21,39-45</sup> and quantitative comparisons of these methods to full QM methods are needed to explore their effectiveness.

The QM/MM nanotubes were approximately 85.0 Å in length. The [5,5] nanotubes contained 700 atoms, the [10,0] contained 820 atoms. In both cases, the ends of the tubes were capped by hydrogen atoms. The two-atom vacancy defect was created by removing two adjacent atoms and the resulting 14 atom ring reconstructs to form one octagon and two pentagons as shown in Fig. 1(a). Two-atom vacancy defects can be produced in CNTs by irradiation with energetic ions or electrons.<sup>46,47</sup> Figure 2 shows the QM fragment in the center of a [10,0] CNT surrounding the two-atom vacancy defect. The QM fragment covers a circular band around the entire circumference of the CNT, so that no QM bonds are stressed in parallel with the MM bonds.

Figure 3 shows the stress-strain curves for a [10,0] CNT with a two-atom vacancy calculated by the QM/MM method with increasing fragment sizes, along with the QM results of a CNT containing 198 atoms calculated by Mielke *et al.*<sup>6,48</sup> and the scaled and unscaled MM results. In the scaled MM calculations, the energy was scaled by the same factor as in the QM/MM calculations. The scaled MM results compare quite well with the QM and QM/MM results. In the QM/MM calculations, the largest quantum fragment is a 158 atom cylindrical band. It can be seen that for the 158 atom fragment, the stress-strain curve for the QM/MM calculations

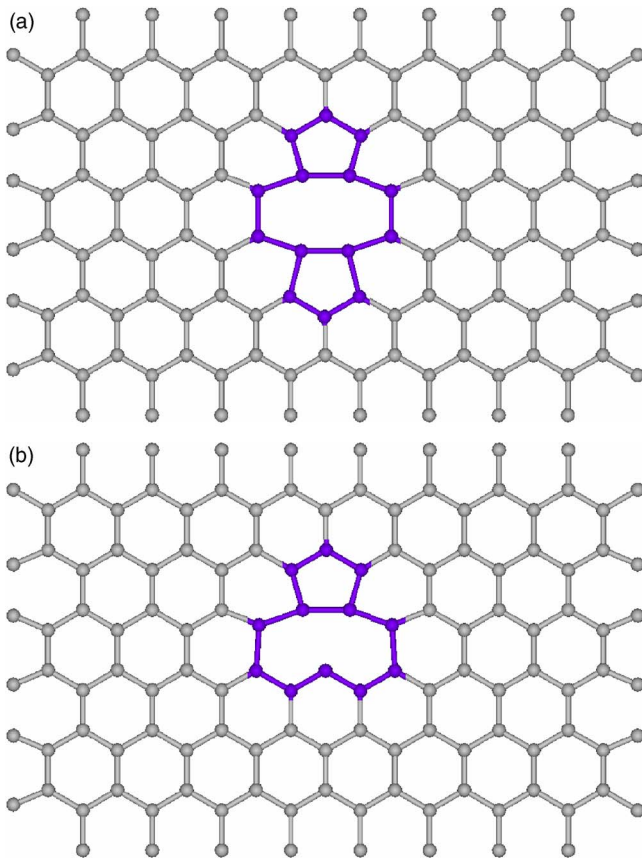


FIG. 1. (Color online) (a) Two-atom and (b) one-atom vacancy defects shown on a graphene sheet.

agrees well with the full QM calculations. The major discrepancy is that the QM/MM model fails at somewhat smaller strain (0.130 versus 0.142) and somewhat smaller stress (103 GPa versus 107 GPa) than the QM model. Undoubtedly, an even larger fragment would compare better with the full QM treatment, but we deemed the 158 atom fragment adequate for our purposes.

It is noteworthy that the QM/MM model, like the full QM model, can sustain larger strains and stresses than the MM model, and fracture always initiates in the QM region. The scaled and unscaled MM models failed at a strain of 0.085, whereas for QM and QM/MM models fracture strain was greater than 0.130. A complication that arises for QM fracture studies of finite-sized CNTs is that Peierls distortions<sup>49,50</sup> can lead to distorted bond lengths as a function of the position along the tube axis and this can result in multiple fracture pathways.<sup>6</sup> These are purely quantal effects that have a very strong size dependence so they are difficult to model precisely by QM/MM methods.

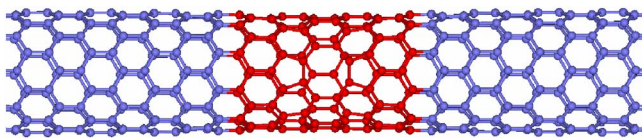


FIG. 2. (Color online) Coupled QM/MM model: the central region constitutes the QM fragment (QM atoms, dark red dots; MM atoms, light blue dots).

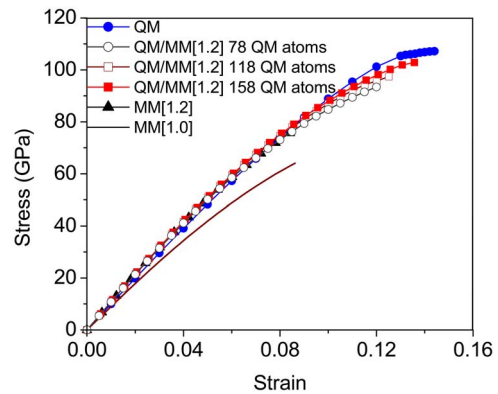


FIG. 3. (Color online) Stress-strain curves of [10,0] CNT with a two-atom vacancy. PM3 was used for the QM/MM and QM calculations. The scaling factor used for the MM potential is given in the square brackets. The QM results were taken from Mielke *et al.* (Ref. 6) and Troya *et al.* (Ref. 48).

Figure 4 shows the stress-strain curves for a [5,5] CNT containing a one-atom vacancy. It can be seen that with the different scaling of the MM energy for the armchair CNT, we were able to replicate full QM results<sup>6,48</sup> quite well with the QM/MM model. Again, the scaled MM results also match the QM and QM/MM results quite well, although the fracture strain is somewhat lower: 0.117 by molecular mechanics versus 0.153 by quantum mechanics.

Table I lists the fracture stresses and strains calculated for these CNTs along with the corresponding values for the pristine tubes reported in Mielke *et al.*<sup>6</sup> In the [10,0] CNTs, the QM/MM failure stress is about 6% below the QM fracture stress, whereas for the [5,5] CNTs they are 3 to 5% higher. The unscaled MM fracture stresses are significantly lower, especially for zigzag CNTs, where the difference is about 40%. With the scaling, the agreement improves and the differences are about 25%.

A noteworthy difference between the QM/MM and the scaled MM computations is that the CNTs can be stretched to

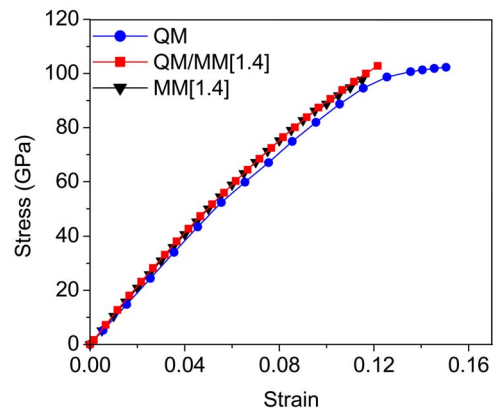


FIG. 4. (Color online) Stress-strain curves of [5,5] CNT with a one-atom vacancy. The QM subdomain consisted of 89 atoms. PM3 was used for the QM/MM and QM calculations. The scaling factor used for the MM potential is given in the square brackets. The QM results were taken from Mielke *et al.* (Ref. 6) and Troya *et al.* (Ref. 48).

TABLE I. Fracture properties calculated using pure QM, QM/MM, and MM methods. All stresses are in GPa. All of the QM results were taken from Mielke *et al.* (Ref. 6) and Troya *et al.* (Ref. 48). PM3 was used for all the QM/MM calculations. Scaling factors of 1.2 and 1.4 were used for [10,0] and [5,5] CNTs, respectively, for all of the QM/MM calculations and the scaled MM calculations. Note that the fracture strain for the scaled and unscaled MM calculations are the same. Also note that we do not report the QM/MM strengths of pristine CNTs, as they fractured at the QM/MM interface or in the MM region.

Chirality	Defect	QM atoms in QM/MM	QM stress	QM/MM stress	Scaled MM stress	MM stress	QM strain	QM/MM strain	MM strain
[10,0]	Pristine		124		106	88	0.20		0.181
[10,0]	Two-atom vac. sym.	158	107	103	77	64	0.142	0.130	0.085
[10,0]	One-atom vac.	119	101	95	78	65	0.130	0.122	0.089
[5,5]	Pristine		135		147	105	0.30		0.297
[5,5]	Stone-Wales	120	125	131	123	88	0.22	0.186	0.162
[5,5]	One-atom vac.	89	100	103	99	71	0.153	0.121	0.117

higher strains in the QM/MM model than in the MM model. Consequently, the QM/MM calculations predict higher fracture strain but similar values of Young's modulus as the scaled MM model. On comparing the results of coupled QM/MM and MM calculations, we found that in the former the bonds at the edge of the defect are able to sustain much larger strains. It can be seen from Figs. 3 and 4 that there is little difference in the initial slopes of the stress-strain curves, i.e., in Young's modulus, between the QM/MM and scaled MM calculations.

We also studied the convergence of pure QM calculations with model size for the same system as was presented in Fig. 3. Calculated failure stresses obtained with 118 and 158 atom models both agreed with the 198 atom model to within 1 GPa. This shows that the ONIOM based QM/MM algorithm with hydrogen link atoms tend to the long cylinder solution more slowly than pure QM calculations for the special case where the QM subdomain consists of a cylindrical section of a nanotube. We have only noticed this effect for calculations where the QM region consists of cylindrical subdomains. Additionally, pure QM calculations are not affordable for the larger tubes that we consider next, so QM/MM calculations provide the only practical scheme for including quantum effects in fracture studies in models of these sizes.

### B. Slits and hexagonal and circular hole defects

We next consider the effect of larger defects on the strength of CNTs. Both slit-like and hole defects were studied. We chose slits because crack-like defects are not readily amenable to QM treatments. In MM calculations, cracks are customarily modeled by artificially removing a single row of bonds. This is not feasible quantum mechanically because unless the atoms adjacent to the crack are separated by a significant distance, the bonds persist, i.e., a loss of cohesion between atoms only occurs at a significant separation, which is much greater than the lattice constant.

This observation also has significant implications for actual cracks at the nanoscale, as it suggests that crack-like defects cannot exist in an unstressed covalently-bonded material unless at least one row of atoms is absent or the crack

surfaces become chemically modified. Thus, the notion of atomistically sharp cracks and MM models with cracks represented by simply omitting bonds must be considered very carefully.

The hole defects were formed by removing hexagonal units of atoms as presented previously<sup>6,14</sup> (see Fig. 5). We denote the size of the hole by a size index: a zero index hole is created by removing one hexagonal unit, a hole of index one is created by removing a ring of six hexagonal units surrounding this hexagon, a hole of index  $n$  by removing the  $n$ th ring of hexagonal units.<sup>6,14</sup> In a zigzag tube, circumferential slit defects are created by removing four rows of carbon atoms as shown in Fig. 5(c), whereas in an armchair CNT, slit defects are created by removing three rows of carbon atoms as shown in Figs. 5(d) and 5(e). For both zigzag and armchair CNT, the size index for a slit is defined so that a slit of index  $n$  is of the same length as the diameter of a hole of index  $n$ . Note that the holes are created in the same way for both the zigzag and armchair tubes, i.e., by removing hexagonal units of atoms, whereas construction of the slit defects is different. Also note that a zero index hole is identical to a zero index slit. Figure 5 shows holes and slits of indices zero and one in a zigzag CNT and slits of indices one and two in an armchair CNT. In all cases, the dangling bonds at the hole/slit edges were terminated with hydrogen atoms so as to create defects with plausible bonding structures as shown in Fig. 5.

We considered [50,0] and [29,29] CNTs containing  $\sim 4000$  atoms which were 94.5 and 83.6 Å long, respectively. Using a quantum fragment which covers the entire circumference for such large CNTs is computationally too expensive, so patch-shaped quantum fragments were used instead, an example of which is shown in Fig. 6. The QM patches used for small slits are shown in Fig. 5.

Using the QM/MM method, the fracture stresses of [50,0] CNTs with holes of size index zero to four and slits of size index zero to eight were calculated (see Fig. 7). These results show that the fracture strengths for holes and slits with the same size indices, i.e., where the length of the slit is equal to the diameter of the hole, differ by less than 5%. Similar agreement between fracture stresses of holes and slits was obtained by molecular mechanics.<sup>14</sup> This is in stark contrast to continuum mechanics at the macroscale, where the weak-

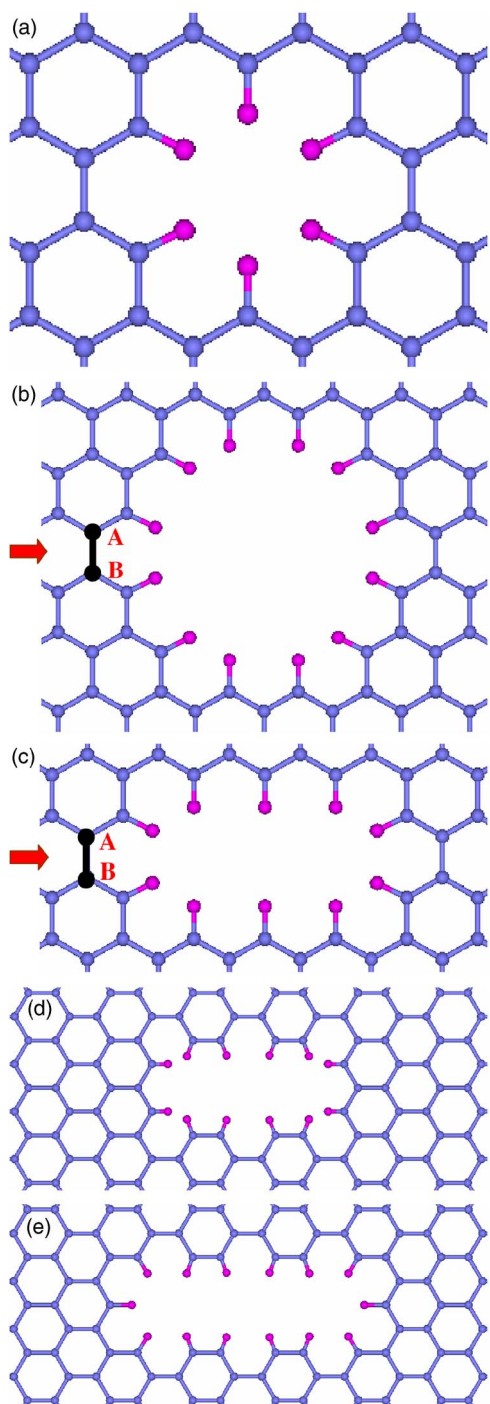


FIG. 5. (Color online) Hole and circumferential slit defects in CNTs (carbon, light blue dot; hydrogen, dark pink dot). (a) A slit or hole of index zero, (b) hole of index one, and (c) slit of index one in a zigzag CNT; (d) a slit of index one (e) and two in an armchair CNT. Local strains are calculated for the bonds in black, shown by red arrows in (b) and (c).

ening effect of holes is much less than the weakening effects of cracks (i.e., slits). To ensure that the small differences in fracture stresses of the holes and slits of the same defect indices are not due to differences in the sizes of the quantum fragments, the fracture stresses of slits of index one and two for a [50,0] CNT were calculated using a quantum fragment

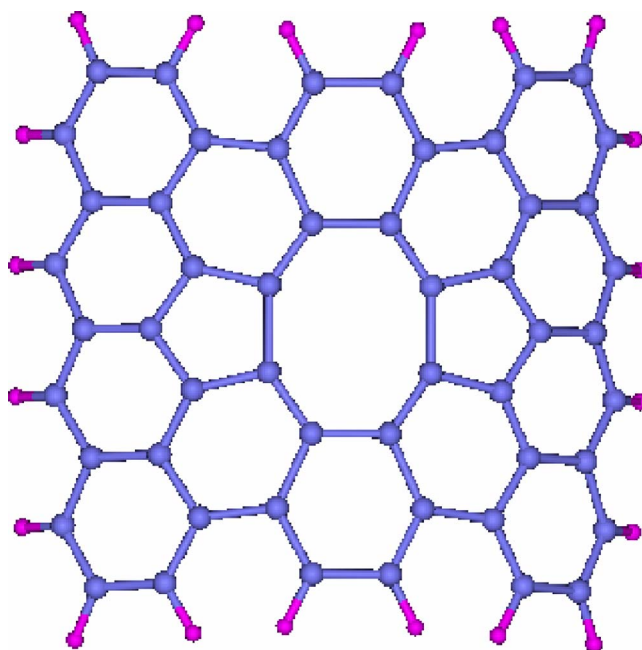


FIG. 6. (Color online) A patch quantum subdomain for a [29,29] CNT containing a two-atom vacancy defect(carbon, light blue dot; hydrogen, dark pink dot).

of the same size as for the corresponding holes. The computed strength, as can be seen from Fig. 7 and also tabulated in Table II, does not change significantly with the QM subdomain size. Note that the MM results have been scaled by the same scaling factor used for the QM/MM calculations. It is observed that even though the fracture stresses obtained by the QM/MM method are higher than those calculated by molecular mechanics, the trend of the fracture stress versus defect size remains the same.

The results for the fracture of defected [29,29] CNTs are shown in Fig. 8. The dependence on defect-size index and the relationship between the scaled MM results and the QM/MM results is similar to what was observed for [50,0]

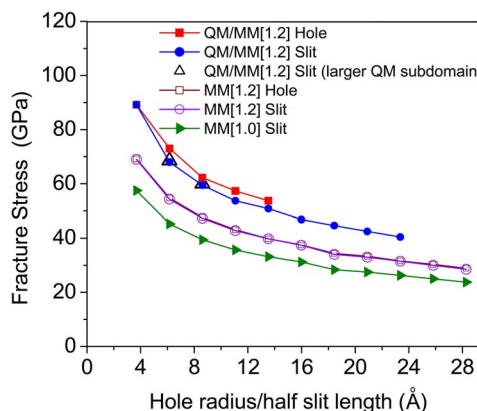


FIG. 7. (Color online) Dependence of the fracture stress of a [50,0] CNT on the defect size for holes and slits. PM3 was used for all the QM/MM calculations. The scaling factor used for the MM potential is given in the square brackets. The MM[1.2] Hole and MM[1.2] Slit results are so close as to be nearly indistinguishable.

TABLE II. Variation of fracture stress and strain of the QM/MM model with QM fragment size for a [50,0] CNT with slits of indices one and two. PM3 was used for all the QM/MM calculations. The MM potential was scaled by a factor of 1.2.

Slit index	Number of atoms in fragment	Fracture stress (GPa)	Fracture strain
1	68	68.0	0.077
1	104	68.6	0.077
2	84	59.5	0.072
2	148	60.0	0.072

CNTs. For armchair tubes, spin-restricted QM calculations predict that a surface perpendicular to the tube axis has the lowest surface energy density (5.39 and 5.44 J/m<sup>2</sup> for PM3 and DFT, respectively) whereas the MM potential predicts a higher surface energy density than was observed for zigzag CNTs (5.09 J/m<sup>2</sup> versus 4.90 J/m<sup>2</sup>). Thus, the fracture within the QM subdomain remains perpendicular to the tube axis but thereafter the fracture surface becomes jagged. Although zigzag tubes have a higher value of  $\gamma$  at the QM level than armchair tubes, the latter possess higher fracture strengths. PM3 calculations for  $\gamma$  are roughly 40% higher for armchair CNTs if fragment relaxation is neglected whereas in zigzag tubes neglecting fragment relaxation produces  $\gamma$  values that are only a few percent higher. In the relaxed armchair CNT fragments, the C–C bonds along the newly created surface have bond lengths of  $\sim 1.2$  Å and are reminiscent of the triple bonds observed in benzyne. These results suggest that fracture for armchair CNTs will display a significant lattice trapping effect. The correlation between large surface relaxation and large lattice trapping effects has already been observed in SiC fracture by Perez and Gumbsch.<sup>51</sup>

In order to develop an understanding of the differences between the QM/MM and MM predictions of fracture, we studied the elongation of the bonds which break first and initiate the fracture. For the hole and slit of index one in a

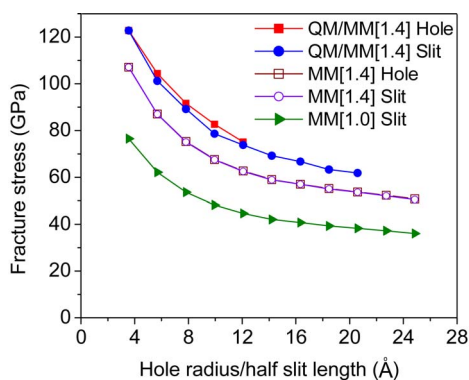


FIG. 8. (Color online) Dependence of the fracture stress of a [29,29] CNT on the defect size for holes and slits. PM3 was used for all the QM/MM calculations. The scaling factor used for the MM potential is given in the square brackets. The MM[1.4] Hole and MM[1.4] Slit results are so close as to be nearly indistinguishable.

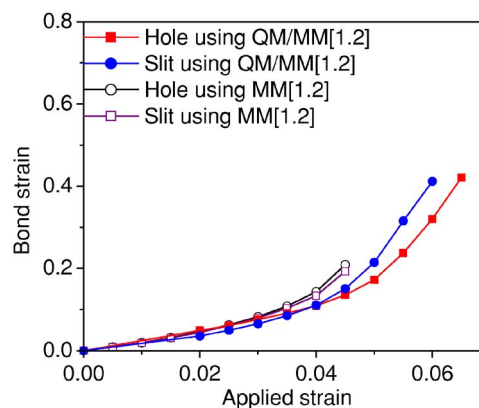


FIG. 9. (Color online) Strain in the bond at the fracture initiation site calculated for a slit and hole of index one in a [50,0] CNT using MM and QM/MM models. PM3 was used for the QM/MM calculations. The scaling factor used for the MM potential is given in the square brackets.

[50,0] CNT, these bonds are labelled AB in Fig. 5. The strain in these bonds for QM/MM and MM calculations are plotted versus applied axial strain in Fig. 9. It can be seen that the strain in the bond that fails is much higher than the applied strain due to the strain concentration at the defect tip. The bond strains obtained by the MM and the QM/MM calculations vary almost identically until the applied strain reaches 4.5%, at which point the bond AB in the MM model breaks. In the next strain increment, catastrophic fracture breaks the tube into two pieces. On the other hand, in the coupled model, where the critical bond is treated quantum mechanically, bond AB stretches to a larger strain without breaking. This is a major difference between the behavior of the MTB-G2 potential and the QM calculations: quantum mechanically bonds around a defect can stretch much more without breaking, thus resulting in higher fracture strains and somewhat higher fracture stresses. It is of interest that the behavior of the bond that breaks first is similar in slits and holes; this is true for both the molecular mechanics and the coupled model.

The holes in the preceding studies are hexagonal rather than circular. We also generated some holes with the same opening size normal to the direction of loading but with a more circular shape. Figure 10 shows this kind of hole defect of size index 10 in a graphene sheet. Fracture stresses were calculated for such circular holes with indices six to eight using MTB-G2 in a [50,0] CNT (defects with size-index  $\leq 5$  are already as circular as possible). The results are given in Table III. Even though the amount of material removed in the hexagonal opening is less than in the circular opening, the strength of CNTs with circular hole defects is about 40% larger. Thus, it is apparent that the corner, labelled C in Fig. 10(a), results in a significant decrease in strength. If, as seen from the results in Table III, two extra carbon atoms are added to the corners of the hexagonal holes to blunt the fracture initiation site, the fracture strength increases to nearly that observed in the rounded holes. Thus, the shape of the defect at the fracture initiation site and the cross section of the defect perpendicular to the loading direction are the key features determining the fracture strength.

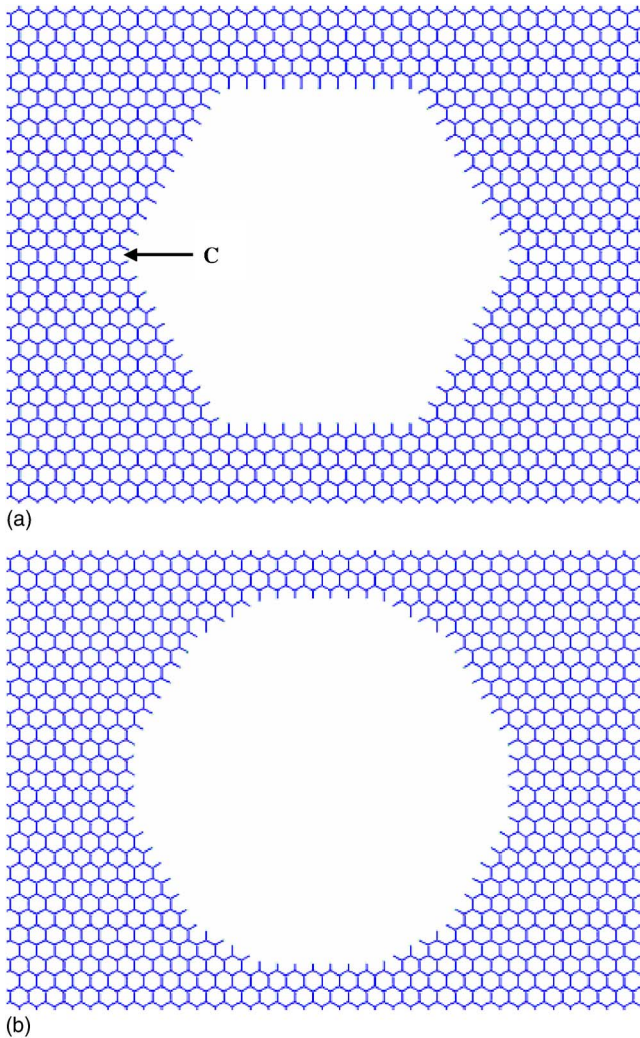


FIG. 10. (Color online) (a) A hexagonal hole and (b) a circular hole of size index 10 in a graphene sheet. C indicates a corner of the hexagonal hole.

Next we compared the fracture stresses calculated using the coupled method with the Griffith formula stress  $\sigma_f$  [Eq. (4)] for slits in a finite graphene sheet. We considered graphene sheets, which have similar bonding as CNTs, because long slits can be modeled more easily in the sheets. To avoid any effects due to the finite-size of the graphene sheets, Mattoni *et al.*<sup>37</sup> suggested that the length and width of

TABLE III. Fracture stresses calculated using molecular mechanics for slits, hexagonal holes, and circular holes for a [50,0] CNT. The blunted hexagonal holes were created by adding two extra carbon atoms to the corners of the hexagonal holes. All stresses are in GPa.

Size index	Slit	Hexagonal hole	Circular hole	Blunted hexagonal hole
6	28.3	28.7	40.5	37.6
7	27.5	27.8	38.0	36.7
8	26.2	26.3	36.7	34.7

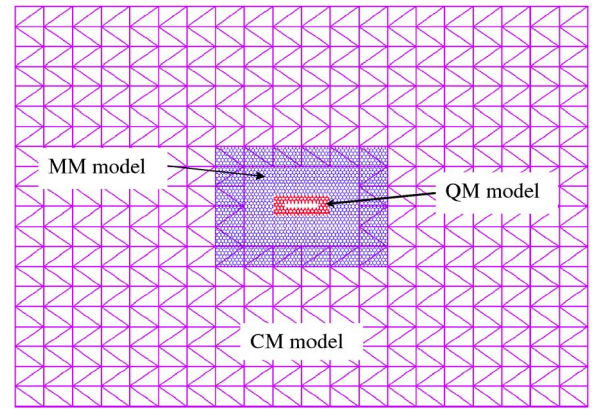


FIG. 11. (Color online) A coupled QM/MM/CM model.

the sheet should be more than five times the crack length. To simulate such big sheets we coupled our atomistic model with a continuum mechanical (CM) model using an overlapping domain-decomposition scheme, known as the bridging domain method.<sup>52,53</sup> In this method, a linear-elastic finite-element model is used for the continuum representation. The constraints on the displacements in the continuum-atomistic overlapping domain are imposed by the Lagrange-multiplier method. Quantum mechanics was applied on a small region surrounding the slit and the coupled continuum-atomistic model was applied elsewhere as shown in Fig. 11. The dimensions of the full sheet were  $393.5 \text{ \AA} \times 411.8 \text{ \AA}$ , where the atomistic region was  $115.5 \text{ \AA} \times 82.3 \text{ \AA}$ , and located in the center of the sheet. A rectangular patch containing the slit was chosen as the QM fragment, as shown in Fig. 5 for small slits.

The results computed by the QM/MM/CM method decrease roughly well with the inverse of the square root of the crack length. Furthermore, they agree quite well with the predictions of the Griffith formula, Eq. (4). Thus, it can be inferred that continuum fracture mechanics agrees quite well with electronic structure calculations for defects as small as  $\sim 10 \text{ \AA}$ . Mattoni *et al.*<sup>37</sup> obtained an even better agreement between the Griffith formula and molecular mechanics calculations on SiC with a Tersoff model.

Although the Griffith stress is a rigorous lower bound on the fracture stress, the approximate stress estimate of the Griffith formula [Eq. (4)] need not be, and as seen in Fig. 12 it predicts results somewhat above the numerical ones for slits shorter than about  $20 \text{ \AA}$ . However, the shape of such small slits, as can be seen from Fig. 5(a), bears little relationship to what is commonly called a crack, so the inadequacy of the Griffith formula for small slits is not surprising.

These results are somewhat in disagreement with the arguments of Gao *et al.*,<sup>54</sup> who propose that materials are defect tolerant at the nanoscale and that there is little difference between the theoretical strength and the strength of perfect crystals in the presence of cracks less than  $30 \text{ nm}$  in length. However, here we observe that the fracture stresses decrease monotonically and sharply from the pristine strength of  $\sim 115 \text{ GPa}$  as the defect size increases. The computed strengths displayed in Fig. 12 are within 10% of the Griffith formula results for slits as short as  $20 \text{ \AA}$ . This supports the arguments in Ballarini *et al.*<sup>55</sup>

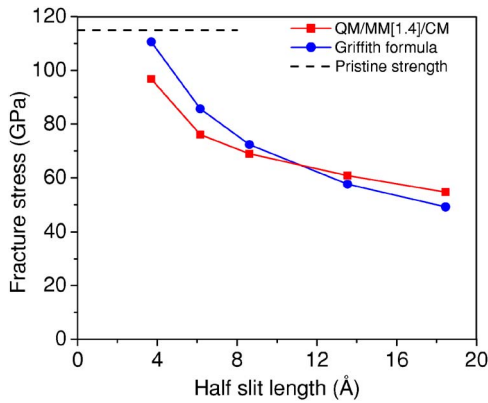


FIG. 12. (Color online) The fracture stress of a graphene sheet, containing slits, and strained in a direction perpendicular to the zigzag edge, calculated using the QM/MM/CM method, and compared to results of the Griffith formula. PM3 was used for the QM/MM/CM calculations. The scaling factor used for the MM potential is given in the square brackets.

#### IV. LATTICE TRAPPING FOR GRAPHENE SHEETS

An interesting question concerning fracture at the nanoscale is whether it differs markedly from fracture at the macroscale. The major assumptions in the derivation of the Griffith formula that do not apply to graphitic materials are:

- (1) The linearity of the stress-strain law.
- (2) Constant energy release, i.e., the neglect of lattice trapping.

The stress-strain law for graphitic materials is somewhat nonlinear, as is apparent from Figs. 3 and 4. Here we examine the extent to which lattice trapping plays a role in the fracture of graphene.

Omel'tchenko *et al.*<sup>56</sup> used molecular dynamics to study crack-front propagation in graphene and calculated fracture toughness in terms of a stress intensity factor (note, however, that retention of the REBO cutoff function makes the quan-

titative aspects of these results questionable). We will calculate the energy release rate,  $J$ , and compare it to twice the surface energy density. The difference is indicative of the magnitude of lattice trapping: in the absence of lattice trapping, the energy release rate at the point of fracture should equal twice the surface energy density.

To simulate a crack growth process that matches notions of a crack as closely as possible, we apply a crack-opening displacement to the boundary of a pristine specimen. A QM fragment is placed at the center, surrounded by an MM model as shown in Fig. 13. We use a displacement field<sup>35</sup> given by

$$u_x = \frac{K_I}{2\mu} \sqrt{\frac{r}{2\pi}} \cos \frac{\theta}{2} \left[ (\kappa - 1) + 2 \sin^2 \frac{\theta}{2} \right] \quad (5)$$

and

$$u_y = \frac{K_I}{2\mu} \sqrt{\frac{r}{2\pi}} \sin \frac{\theta}{2} \left[ (\kappa + 1) - 2 \cos^2 \frac{\theta}{2} \right], \quad (6)$$

where  $u_x$  and  $u_y$  are the displacements in the  $x$  and  $y$  directions, respectively,  $\mu$  is the shear modulus of the material [which can be expressed in terms of Young's modulus,  $Y$ , and Poisson's ratio,  $\nu$ , as  $\mu = Y/2(1+\nu)$ ],  $\theta$  and  $r$  are the cylindrical coordinates measured from the crack tip and  $\kappa = (3-\nu)/(1+\nu)$  for plane stress. The appropriate continuum model for a monolayer graphene sheet is a state of plane stress.

The parameter  $K_I$ , which corresponds to the mode I stress intensity factor, is then incremented until a crack develops along the segment  $x < 0$ , see Fig. 13. An interesting feature of this loading is that because of its antisymmetry the bonds are broken sequentially in order of increasing  $x$ . Thus, the crack grows from left to right, and for sufficiently large  $K_I$  all bonds for  $x < 0$  break.

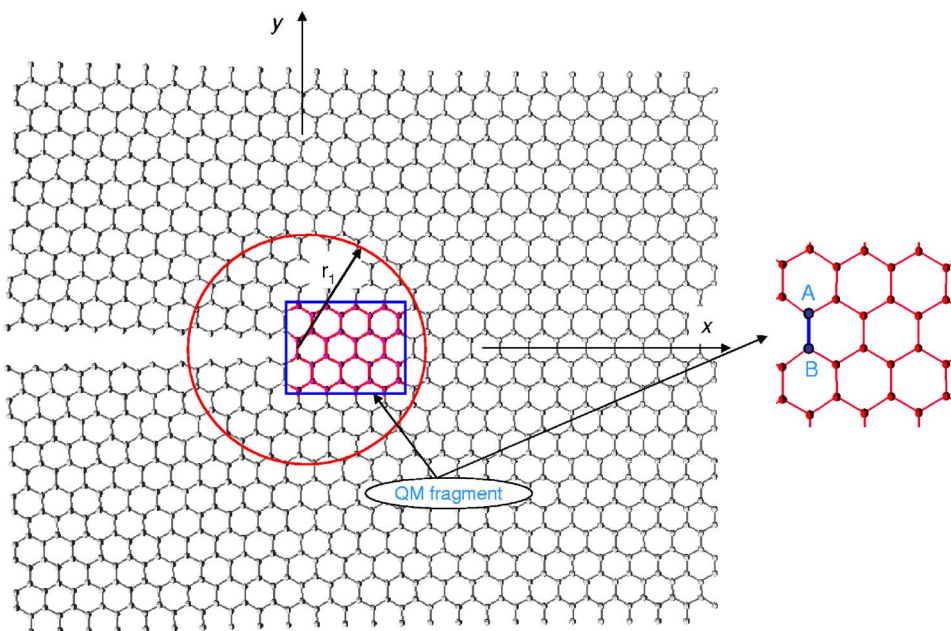


FIG. 13. (Color online) A graphene sheet containing a crack. The quantum fragment is shown in the inset. The bond A-B forms the crack tip. Note that  $r_1$  is large enough to enclose the quantum fragment.

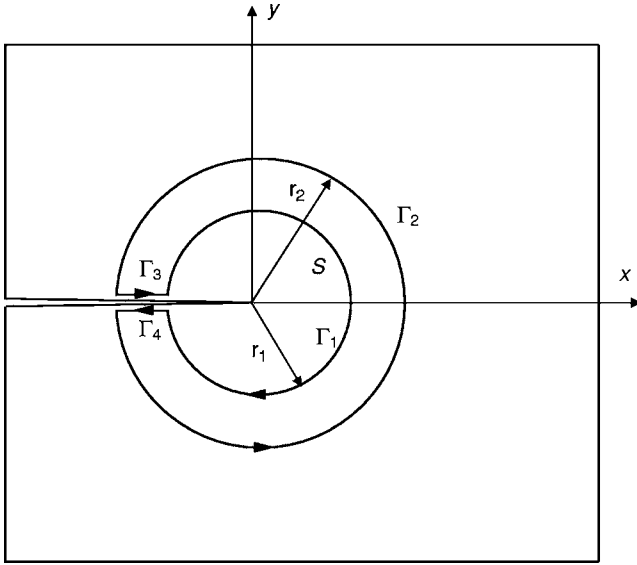


FIG. 14. Closed contour around a crack tip.

We calculated the energy release rate by a discrete form of the energy release<sup>57</sup> integral (a domain form of the Rice  $J$  integral<sup>22</sup>);

$$J = \int_{S_0} \sum_{i,j}^2 \left[ \left\{ W \delta_{ij} - P_{ij} \frac{\partial u_i}{\partial X_1} \right\} \frac{\partial q}{\partial X_j} \right] dS, \quad (7)$$

where  $W$  is the strain energy density,  $\mathbf{P}$  is the first Piola-Kirchhoff stress tensor,  $\mathbf{u}$  is the displacement field,  $\mathbf{X}$  are the material coordinates,  $S_0$  represents the undeformed area of the domain,  $\delta$  is Kronecker delta, and

$$q = \begin{cases} 0 : r = r_1, \\ 1 : r = r_2, \\ (r - r_1)/(r_2 - r_1) : \text{otherwise,} \end{cases} \quad (8)$$

where  $r_1$  and  $r_2$  are as shown in Fig. 14. The discrete form of Eq. (7) (the form for small displacements reported previously<sup>58,59</sup>) is given by

$$J = \sum_{\alpha \in S_0} \sum_{i,j}^2 \left[ \left\{ W^\alpha \delta_{ij} - P_{ij}^\alpha \frac{\partial u_i(\mathbf{X}_\alpha)}{\partial X_1} \right\} \frac{\partial q(\mathbf{X}_\alpha)}{\partial X_j} \right] S_0^\alpha, \quad (9)$$

where  $S_0^\alpha$  is the initial undeformed area occupied by the atom  $\alpha$ ,  $\mathbf{X}_\alpha$  is the initial position of atom  $\alpha$ ,  $W^\alpha$  is the local strain energy density at any atom  $\alpha$  which is calculated by the expression

$$W^\alpha = \int_0^{\epsilon_{ij}} \sum_{i,j}^2 P_{ij}^\alpha d\epsilon_{ij}^\alpha, \quad (10)$$

and the stress at the atom  $\alpha$  ( $\mathbf{P}^\alpha$ ) is calculated by the virial stress definition<sup>60</sup>

$$\mathbf{P}^\alpha = \frac{1}{2\Omega_\alpha} \sum_{\beta \neq \alpha} \mathbf{r}^{\alpha\beta} \otimes \mathbf{f}^{\alpha\beta}, \quad (11)$$

where  $\mathbf{r}^{\alpha\beta}$  is a vector joining atoms  $\alpha$  and  $\beta$ ,  $\mathbf{f}^{\alpha\beta}$  is the force applied on atom  $\alpha$  by atom  $\beta$ , and  $\Omega_\alpha = S^\alpha t$  is the volume

TABLE IV. Critical energy release rate compared to twice the surface energy density for graphene strained in a direction perpendicular to the zigzag edge. All the values are in  $\text{J/m}^2$ . The scaling factor used for the MM potential is given in the square brackets.

Method	$J_{IC}$	$2\gamma$	$J_{IC}/2\gamma$
QM(DFT)/MM[1.2]	14.5	13.2	1.1
QM(PM3)/MM[1.4]	15.8	13.4	1.2
MM[1.2]	13.0	11.8	1.1
MM[1.4]	15.1	13.7	1.1
MM	10.8	9.8	1.1

occupied by atom  $\alpha$ , where  $S^\alpha$  is the area occupied by the atom  $\alpha$  in the current configuration.  $S^\alpha$  is obtained by dividing the current area of the domain by the number of atoms in the domain. The virial stress definition for angle bending has been derived in Zhang *et al.*<sup>52</sup> The strain  $\epsilon_{ij}^\alpha$  in Eq. (10) and  $\partial u_i / \partial X_1$  in Eq. (9) were obtained by a moving least square fit to the displacement field.<sup>52,61</sup> Since it is difficult to calculate the bond forces in the QM fragment, we used a domain that lies entirely in the MM region, as shown in Fig. 13, to calculate the  $J$ -integral.

The results are summarized in Table IV. It can be seen that the difference between the  $J$ -integral and twice the surface energy density is only modest for QM/MM calculations using DFT, suggesting a moderate amount of lattice trapping. For the QM(DFT)/MM model  $J_{IC}/2\gamma$  differs from unity by 10%, for the QM(PM3)/MM model and the MM model, this value is 18% and 10%, respectively. These differences between the energy release rates and  $2\gamma$  are marginally significant, as the resulting fracture stresses only change by  $\sqrt{J/2\gamma}$ . Bernstein and Hess<sup>21</sup> have previously reported  $J/2\gamma$  values between 1.19 and 1.35 for silicon (which has similar chemical bonding to that of carbon) when the interactions are calculated via tight binding and much larger values for empirical potentials.

## V. CONCLUDING REMARKS

We have studied the impact of large defects on the strength of carbon nanotubes using a coupled QM/MM method. Both slit-like defects and holes were considered. We found that the strengths of CNTs did not depend strongly on the shape of the defects, i.e., the strengths of CNTs with slit-like and hexagonal hole defects of the same size index are comparable while those with rounder holes were about 40% stronger. This contrasts markedly with the effects of holes and cracks at the macroscale, where the cracks have far more deleterious effects on strength than holes.

Comparison of the fracture strengths with the Griffith formula for slits in a finite graphene sheet shows reasonable agreement (within 10% for the longest cracks we calculated). This is somewhat surprising since the stress-strain law is quite nonlinear and the Griffith formula assumes linear material response. The results indicate that continuum fracture mechanics is applicable to crack-like defects as small as 10 Å. Furthermore, they do not indicate any flaw tolerance to

nanoscale (5–20 nm) defects: for any defect, the strength is below the theoretical strength, as would be expected.

Crack-like defects, which we called slits, were constructed by removing four rows of carbon atoms in the zigzag CNTs and by removing three rows of carbon atoms in the armchair CNTs. The resulting dangling bonds were capped with hydrogen atoms. This is to be contrasted with crack models based on omitting bonds between adjacent atoms in MM calculations, which are pervasive in the literature. Such defects cannot exist in electronic structure models because interactions between nearby atom pairs cannot simply be neglected at moderate distances. Thus, the ability of such schemes to accurately model crack behavior is questionable. Crack-like defects can be formed by displacing a lattice according to the asymptotic near-field of elastic fracture mechanics, as we reported in Sec. IV. However, such cracks will not exist in a solid in a stress-free state.

To ascertain the magnitude of lattice trapping in graphene, we computed the energy release rate using a discrete  $J$ -integral and compared it to twice the surface energy density,  $2\gamma$ . These results indicate a modest amount of lattice trapping; the energy release rate calculated by DFT for a graphene sheet at fracture exceeds  $2\gamma$  by 10%.

The coupled QM/MM calculations were performed with the ONIOM methodology. We checked the accuracy of the method by performing a series of calculations for small defects with QM fragments of increasing size. The resulting stress-strain curves agreed closely over most of the range even for relatively small QM fragments. The fracture stresses and strains also appear to converge, but are more sensitive to the QM fragment size and even for the largest two fragments studied, the fracture stresses and strains differed from the pure QM results by 4% and 8%, respectively, for a [10,0] CNT with a two-atom vacancy defect. Thus, the absolute

accuracy of the coupled QM/MM calculations for the failure stress is probably only a few percent and the results are more useful for comparing defects of various sizes than in obtaining quantitative values of failure stresses.

We introduced a simple scaling scheme to improve the compatibility of the MM and QM models. If the MM interaction potential is used unscaled, mismatches between the stiffness and strength of the MM and QM subdomains result in highly spurious behavior. Comparisons of the QM/MM calculations with MM calculations using the scaled potential show good agreement for the failure stresses and stress-strain curves. In most cases, the differences were less than 15%, and the qualitative pattern of dependence on defect size agreed well. It should be noted that this good agreement is only achieved for the scaled MM potential. The details of the fracture processes predicted by the QM/MM method and the MM method differ significantly. For example, QM/MM calculations show significantly more elongation of the bond at the crack tip.

The results provide further credence to the hypothesis<sup>6</sup> that large defects such as holes are the reason behind the low CNT fracture strengths observed in some experiments.<sup>12</sup> Although the QM/MM models predict failure stresses that are about 40% higher than unscaled MM results modeled previously,<sup>6,14</sup> they are still in the range observed in the Yu *et al.* experiments.<sup>12</sup>

#### ACKNOWLEDGMENTS

We thank Diego Troya for helpful conversations. We gratefully acknowledge grant support from the NASA University Research, Engineering and Technology Institute on Bio Inspired Materials (BIMat) under award No. NCC-1-02037, from the Army Research Office under Grant No. W911NF-05-1-0049, and from the National Science Foundation.

\*Electronic address: schatz@chem.northwestern.edu

†Electronic address: tedbelytschko@northwestern.edu

<sup>1</sup>T. Ozaki, Y. Iwasa, and T. Mitani, Phys. Rev. Lett. **84**, 1712 (2000).

<sup>2</sup>T. Dumitrica, T. Belytschko, and B. I. Yakobson, J. Chem. Phys. **118**, 9485 (2003).

<sup>3</sup>D. Troya, S. L. Mielke, and G. C. Schatz, Chem. Phys. Lett. **382**, 133 (2003).

<sup>4</sup>S. Ogata and Y. Shibutani, Phys. Rev. B **68**, 165409 (2003).

<sup>5</sup>G. Dereli and C. Ozdogan, Phys. Rev. B **67**, 035416 (2003).

<sup>6</sup>S. L. Mielke, D. Troya, S. Zhang, J.-L. Li, S. Xiao, R. Car, R. S. Ruoff, G. C. Schatz, and T. Belytschko, Chem. Phys. Lett. **390**, 413 (2004).

<sup>7</sup>T. Dumitrica, M. Hua, and B. I. Yakobson, Proc. Natl. Acad. Sci. U.S.A. **103**, 6105 (2006).

<sup>8</sup>A. G. Rinzler, J. Liu, H. Dai, P. Nikolaev, C. B. Huffman, F. J. Rodriguez-Macias, P. J. Boul, A. H. Lu, D. Heymann, D. T. Colbert *et al.*, Appl. Phys. A: Mater. Sci. Process. **67**, 29 (1998).

<sup>9</sup>R. C. Haddon, J. Sippel, A. G. Rinzler, and F. Papadimitrakopoulos, MRS Bull. **29**, 252 (2004).

<sup>10</sup>Y.-Q. Xu, H. Peng, R. H. Hauge, and R. E. Smalley, Nano Lett.

**5**, 163 (2005).

<sup>11</sup>S. L. Mielke, T. Belytschko, and G. C. Schatz, Annu. Rev. Phys. Chem. **58**, 185 (2007).

<sup>12</sup>M.-F. Yu, O. Lourie, M. J. Dyer, K. Moloni, T. F. Kelly, and R. S. Ruoff, Science **287**, 637 (2000).

<sup>13</sup>H. C. Schniepp, J.-L. Li, M. J. McAllister, H. Sai, M. Herrera-Alonso, D. H. Adamson, R. K. Prud'homme, R. Car, D. A. Saville, and I. A. Aksay, J. Phys. Chem. A **110**, 8535 (2006).

<sup>14</sup>S. Zhang, S. L. Mielke, R. Khare, D. Troya, R. S. Ruoff, G. C. Schatz, and T. Belytschko, Phys. Rev. B **71**, 115403 (2005).

<sup>15</sup>O. A. Shenderova, D. W. Brenner, A. Omeltchenko, X. Su, and L. H. Yang, Phys. Rev. B **61**, 3877 (2000).

<sup>16</sup>T. Belytschko, S. P. Xiao, G. C. Schatz, and R. S. Ruoff, Phys. Rev. B **65**, 235430 (2002).

<sup>17</sup>D. W. Brenner, O. A. Shenderova, J. A. Harrison, S. J. Stuart, B. Ni, and S. B. Sinnott, J. Phys.: Condens. Matter **14**, 783 (2002).

<sup>18</sup>R. Thomson, C. Hsieh, and V. Rana, J. Appl. Phys. **42**, 3154 (1971).

<sup>19</sup>J. R. Rice, J. Mech. Phys. Solids **26**, 61 (1978).

<sup>20</sup>W. A. Curtin, J. Mater. Res. **5**, 1549 (1990).

<sup>21</sup>N. Bernstein and D. W. Hess, Phys. Rev. Lett. **91**, 025501 (2003).

- <sup>22</sup>J. R. Rice, *J. Appl. Mech.* **35**, 379 (1968).
- <sup>23</sup>M. Svensson, S. Humbel, R. D. J. Froese, T. Matsubara, S. Sieber, and K. Morokuma, *J. Phys. Chem.* **100**, 19357 (1996).
- <sup>24</sup>M. W. Schmidt, K. K. Baldrige, J. A. Boatz, S. T. Elbert, M. S. Gordon, J. H. Jensen, S. Koseki, N. Matsunaga, K. A. Nguyen, S. J. Su *et al.*, *J. Comput. Chem.* **14**, 1347 (1993).
- <sup>25</sup>D. Sánchez-Portal, P. Ordejón, E. Artacho, and J. M. Soler, *Int. J. Quantum Chem.* **65**, 453 (1997).
- <sup>26</sup>J. M. Soler, E. Artacho, J. D. Gale, A. García, J. Junquera, P. Ordejón, and D. Sánchez-Portal, *J. Phys.: Condens. Matter* **14**, 2745 (2002).
- <sup>27</sup>N. Troullier and J. L. Martins, *Phys. Rev. B* **43**, 1993 (1991).
- <sup>28</sup>N. Troullier and J. L. Martins, *Phys. Rev. B* **43**, 8861 (1991).
- <sup>29</sup>J. J. Koval, *Appl. Stat.—J. Roy. St. C* **46**, 515 (1997).
- <sup>30</sup>T. Belytschko, W. K. Liu, and B. Moran, in *Nonlinear finite elements for continua and structures* (John Wiley & Sons, New York, 2001).
- <sup>31</sup>M. Arroyo and T. Belytschko, *J. Mech. Phys. Solids* **50**, 1941 (2002).
- <sup>32</sup>M. Arroyo and T. Belytschko, *Int. J. Numer. Methods Eng.* **59**, 419 (2004).
- <sup>33</sup>A. J. Stone and D. J. Wales, *Chem. Phys. Lett.* **128**, 501 (1986).
- <sup>34</sup>A. A. Griffith, *Philos. Trans. R. Soc. London, Ser. A* **211**, 163 (1920).
- <sup>35</sup>T. L. Anderson, *Fracture Mechanics: Fundamentals and Applications* (CRC Press, Boca Raton, 1991).
- <sup>36</sup>D. Vogtenhuber and R. Podlousky, *Phys. Rev. B* **55**, 10805 (1997).
- <sup>37</sup>A. Mattoni, L. Colombo, and F. Cleri, *Phys. Rev. Lett.* **95**, 115501 (2005).
- <sup>38</sup>M. Ippolito, A. Mattoni, L. Colombo, and N. Pugno, *Phys. Rev. B* **73**, 104111 (2006).
- <sup>39</sup>R. E. Rudd and J. Q. Broughton, *Phys. Status Solidi B* **217**, 251 (2000).
- <sup>40</sup>F. F. Abraham, J. Q. Broughton, N. Bernstein, and E. Kaxiras, *Comput. Phys.* **12**, 538 (1998).
- <sup>41</sup>J. A. Moriarty, J. F. Belak, R. E. Rudd, P. Soderlind, F. H. Streitz, and L. H. Yang, *J. Phys.: Condens. Matter* **14**, 2825 (2002).
- <sup>42</sup>A. Mallik, D. E. Taylor, K. Runge, J. W. Dufty, and H. P. Cheng, *J. Comput.-Aided Mater. Des.* **13**, 45 (2006).
- <sup>43</sup>S. Ogata, E. Lidorikis, F. Shimojo, A. Nakano, P. Vashishta, and R. K. Kalia, *Comput. Phys. Commun.* **138**, 143 (2001).
- <sup>44</sup>R. Belkada, T. Igarashi, and S. Ogata, *Comput. Mater. Sci.* **30**, 195 (2004).
- <sup>45</sup>C. L. Rountree, R. K. Kalia, E. Lidorikis, A. Nakano, L. Van Brutzel, and P. Vashishta, *Annu. Rev. Mater. Sci.* **32**, 377 (2002).
- <sup>46</sup>P. M. Ajayan, V. Ravikumar, and J.-C. Charlier, *Phys. Rev. Lett.* **81**, 1437 (1998).
- <sup>47</sup>A. V. Krasheninnikov, K. Nordlund, M. Sirvio, E. Salonen, and J. Keinonen, *Phys. Rev. B* **63**, 245405 (2001).
- <sup>48</sup>D. Troya, S. L. Mielke, and G. C. Schatz (unpublished).
- <sup>49</sup>H. F. Bettinger, *Org. Lett.* **6**, 731 (2004).
- <sup>50</sup>Z. Y. Zhou, M. Steigerwald, M. Hybertsen, L. Brus, and R. A. Friesner, *J. Am. Chem. Soc.* **126**, 3597 (2004).
- <sup>51</sup>R. Pérez and P. Gumbsch, *Phys. Rev. Lett.* **84**, 5347 (2000).
- <sup>52</sup>S. Zhang, R. Khare, and T. Belytschko, *Int. J. Numer. Methods Eng.* (to be published).
- <sup>53</sup>S. P. Xiao and T. Belytschko, *Comput. Methods Appl. Mech. Eng.* **193**, 1645 (2004).
- <sup>54</sup>H. Gao, B.-H. Ji, I. L. Jager, E. Arzt, and P. Fratzl, *Proc. Natl. Acad. Sci. U.S.A.* **100**, 5597 (2003).
- <sup>55</sup>R. Ballarini, R. Kayacan, F. J. Ulm, T. Belytschko, and A. H. Heuer, *Int. J. Fract.* **135**, 187 (2005).
- <sup>56</sup>A. Omeltchenko, J. Yu, R. K. Kalia, and P. Vashishta, *Phys. Rev. Lett.* **78**, 2148 (1997).
- <sup>57</sup>B. Moran and C. F. Shih, *Eng. Fract. Mech.* **27**, 615 (1987).
- <sup>58</sup>K. Nakatani, A. Nakatani, Y. Sugiyama, and H. Kitagawa, *AIAA J.* **38**, 695 (2000).
- <sup>59</sup>Y. Jin and F. G. Yuan, *J. Nanosci. Nanotechnol.* **5**, 2099 (2005).
- <sup>60</sup>A. G. McLellan, *Am. Phys.* **42**, 239 (1974).
- <sup>61</sup>T. Belytschko, Y. Y. Lu, and L. Gu, *Int. J. Numer. Methods Eng.* **37**, 229 (1994).